The International Maritime Transport and Logistics (MARLOG 14) - ISSN 2974-3141
http://dx.doi.org/10.21622/MARLOG.2025.14.1.76
Artificial Intelligence Implementations Towards Shaping the Future of Digital World

DYNAMICS OF OSCILLATING TURBULENT FLOW OVER COASTAL BUILDINGS IN PORTS USING AI TECHNIQUES

Miral Michel (1), Adham Eladly (1), Shehab Mostafa (1), Gerges Refaat (1), Belal Tarek (1), Mohamed Hussein Shokry (1), Mahmoud Ismail (1), Ibraheem Gamal (1) and Ahmed S. Shehata (1)

(1) Marine and Offshore Engineering Department, Arab Academy for Science, Technology and Maritime Transport, Alexandria, Egypt

ABSTRACT

Time-dependent CFD models were used to simulate the flow structures over a square cylinder in oscillating flow. Two-dimensional models were used to study the hydrodynamic forces under sinusoidal flow boundary conditions that were predicted by machine learning algorithms. The study also examines the specifications of the caused entropy around a square cylinder under various conditions, as well as the examination of the second law. It is found that the flow structures and forces values were sensitive to any change in input flow parameter and rotation angle. Furthermore, it is found that the angle 10 degree of rotation object, gives best result for entropy generation in this work.

Keywords: Oscillating Flow, CFD, Vortex Flow Structures, Hydrodynamic Forces, Second Law Analysis.

1. INTRODUCTION

The problem of unsteady flow around coastal buildings is very important from a practical standpoint. Examples of such high Reynolds number flow include chimneys, high-rise buildings, offshore structures, and tube banks in heat exchangers. The requirement to comprehend the wake dynamics behind a stack has increased recently due to the dispersion of pollution. Nonetheless, there are uses for the low Reynolds number flow past a square cylinder in small, compact heat exchangers and electronic chip cooling. Ocean engineers and fluid mechanics researchers have been interested in the unsteady fluid forces acting on bodies in oscillating flow [1], [2], [3], [4], and [5]. The majority of studies have focused on circular cylinders. [6], [7], as well as square or rectangular cylinders [5], [8], [9]. Among the first investigations to determine the drag, inertia, and lift coefficients operating on a circular cylinder positioned at different distances from the bottom in an oscillatory flow were Sarpkaya [10], [11] and Sarpkaya and Rajabi [12]. These force coefficients were determined to depend on the thickness of the boundary layer, the gap-to-diameter ratio, the Reynolds number (Re), and the Keulegan Carpenter (KC) number. The lift force for oscillatory flow over a circular cylinder positioned on a bed was consistently found to be away from the bottom. Liu et al. [13] have conducted a computational investigation of internal flow past a finite circular cylinder with an aspect ratio (AR) of 10. For a range of Reynolds numbers (100 to 200), they documented the production of the necklace or horseshoe vortex at the plate-body junction and the tip vortex at the free-end. Farivar [14] used a hot-film anemometer to experimentally study the turbulent flow past a limited circular cylinder. Three separate vortex rows with varying frequencies are present along the cylinder's length, and the pressure and frequency measurements show a suppressed two-dimensional zone on the lowest portion of the cylinder. The U-shaped oscillating flow tunnel, in which the confined water oscillates at a predetermined natural frequency, is a typical piece of experimental equipment in this field. The resulting flow velocity has a sign that switches cyclically. Its mean velocity then drops to zero. The vortex flow structures and flow turbulence surrounding a 2D square cylinder will be examined using the computational fluid dynamics (CFD) technique. These features are greatly influenced by the

direction and velocity value of sinusoidal oscillating flows, as well as by other parameters like object position angle, axial velocity amplitude, wave flow frequency, object shape, and hydrodynamic forces influenced by those parameters. The paper also studies the second law analysis by the entropy generated around a 2D square cylinder under oscillating flow conditions.

2. METHODOLOGY

2.1. Machine learning model for wind velocity prediction

To enhance the accuracy of wind velocity predictions over coastal buildings, a machine learning (ML) approach was integrated into the computational model. The ML model was trained using historical wind velocity data, numerical simulations, and experimental observations to predict the fluctuating wind speed over different structural geometries.

The dataset consisted of wind velocity measurements obtained from computational fluid dynamics (CFD) simulations which provided detailed insights into the wind flow characteristics around buildings under various oscillatory flow conditions, experimental wind tunnel data where previous studies and real-world measurements of wind velocity over structures in coastal environments were used to validate and refine the model, and meteorological data where historical weather data from coastal regions, including wind speed, direction, temperature, and atmospheric pressure, were incorporated.

The collected data underwent preprocessing steps such as normalization, outlier removal, and feature selection to enhance the model's predictive capabilities.

Several ML algorithms were tested, including:

- Artificial Neural Networks (ANNs): Used for capturing nonlinear relationships between wind parameters.
- Random Forest Regression: Effective for feature importance analysis and robust wind speed estimation.
- Long Short-Term Memory (LSTM) Networks: Employed to capture time-dependent variations in wind velocity.

Based on model performance evaluation, an LSTM network was selected due to its superior accuracy in predicting oscillating wind speeds over time.

The dataset was split into training (70%) and testing (30%) subsets. The model was trained using a mean squared error (MSE) loss function as in Eq. (1) and optimized with the Adam optimizer. Hyperparameter tuning was conducted to refine the network architecture.

$$MSE = \frac{1}{n}\sum_{i=1}^{n}\left(Y_i - \hat{Y}_i\right)^2 \quad (1)$$

Where n is the number of data points, Yi is the observed value, and $\hat{Yi}$ is the predicted value. The trained model was used to predict wind velocity profiles over different coastal building configurations. The predictions were incorporated into the CFD model to adjust boundary conditions dynamically, improving the accuracy of flow simulations. The model was validated against experimental and numerical results, achieving a correlation coefficient (R^2) of 0.94 with CFD-predicted wind velocities. The error margin remained within ±5%, demonstrating the model's reliability in predicting wind oscillations in coastal environments.

2.2. Numerical model

The following governing equations for turbulent, incompressible flow make up the mathematical model [15]. Eq. (2) is the continuity equation while Eq. (3) is the RANS equation.

$$\frac{\partial}{\partial t} + \frac{\partial}{\partial x_i}(\overline{u_i}) = 0 \quad (2)$$

$$\rho\frac{\partial\overline{u_i}}{\partial t}+\frac{\partial}{\partial x_i}\left(\rho\overline{u_i}\overline{u_j}\right)=-\frac{\partial p}{\partial x_j}+\frac{\partial}{\partial x_j}\left[\mu\left(\frac{\partial\overline{u_i}}{\partial x_j}+\frac{\partial\overline{u_j}}{\partial x_i}-\frac{2}{3}\delta_{ij}\frac{\partial\overline{u_j}}{\partial x_i}\right)\right]+\frac{\partial}{\partial x_j}\left(-\overline{\rho u_i' u_j'}\right) \quad (3)$$

The realizable k−ε model, which has the transport equation of kinetic energy (k), is used to create turbulent flow as in Eq. (4).

$$\frac{\partial}{\partial t}(\rho k)+\rho\frac{\partial}{\partial x_i}(U_i K)=\frac{\partial}{\partial x_j}\left[\left(\mu+\frac{\mu_T}{\sigma_k}\right)\frac{\partial}{\partial x_j}k\right]+\mu_T S^2-\rho\varepsilon \quad (4)$$

Specific dissipation rate equation is shown in Eq. (5).

$$\frac{\partial}{\partial t}(\rho\varepsilon)+\rho\frac{\partial}{\partial x_i}(U_i\varepsilon)=\frac{\partial}{\partial x_j}\left[\left(\mu+\frac{\mu_T}{\sigma_\varepsilon}\right)\frac{\partial}{\partial x_j}\varepsilon\right]+C_1\rho S_\varepsilon-C_2\rho\frac{\varepsilon^2}{k+\sqrt{\nu\varepsilon}} \quad (5)$$

Where C_1 is shown in Eq. (6), C_2 = 1.9, and C_μ is shown in Eq. (7).

$$C_1=max\left(0.43,\frac{\eta}{\eta+5}\right) \quad (6)$$

$$C_\mu=\frac{1}{A_o+A_s U^*\frac{k}{\varepsilon}} \quad (7)$$

Where A0 = 0.4, U* is given by Eq. (8), As is given by Eq. (9), W is given by Eq. (10), and the velocity tensor is given by Eq. (11).

$$U^*=\sqrt{S_{ij}S_{ij}+\Omega_{ij}\Omega_{ij}} \quad (8)$$

$$A_s=\sqrt{6}cos\left(\frac{1}{3}arccos\left(\sqrt{6}W\right)\right) \quad (9)$$

$$W=\frac{\sqrt{8}S_{ij}S_{jk}S_{ki}}{S^3} \quad (10)$$

$$\Omega_{ij}=\frac{1}{2}\left(\frac{\partial\overline{u_i}}{\partial x_j}-\frac{\partial\overline{u_j}}{\partial x_i}\right) \quad (11)$$

Where the Reynolds averaged velocity vector is denoted by $\overline{u}$. The Reynolds stress term ($-\rho u'iu'\overline{j}$) of the equation is then solved using one and two-equation turbulence models [16], [17].

The work transfer rate W is indicated by the second rule of thermodynamics in Eq. (12) [18].

$$W=W_{rev}-T_o S_{gen} \quad (12)$$

Regardless of phase transitions and chemical reactions, the irreversible entropy generation can be described in terms of the local flow derivatives. The mechanisms of thermal dissipation and generated dissipation are equivalent to a thermal and a viscous entropy generation, respectively [19]. It can therefore be expressed as in Eq. (13).

$$S_{gen}=S_V+S_{th} \quad (13)$$

The heat dissipation term disappears in incompressible isothermal flow. Thus, the local viscous term can be written as shown in Eq. (14).

$$S_V=\frac{\mu}{T_o}\varphi \quad (14)$$

The global entropy production rate is then written as in Eq. (15), where φ is the viscous dissipation, which is given in two dimensional Cartesian coordinates as in Eq. (16) [19].

$$\varphi=2\left[\left(\frac{\partial u}{\partial x}\right)^2+\left(\frac{\partial v}{\partial y}\right)^2\right]+\left(\frac{\partial u}{\partial y}+\frac{\partial v}{\partial x}\right)^2 \quad (15)$$

$$S_G=\iint_{xy}S_V dydx \quad (16)$$

The axial force coefficient is therefore provided by Eq. (18), and the torque coefficient can be expressed as in Eq. (19) [20].

$$C_T = C_L sin\alpha - C_D cos\alpha \quad (18)$$

$$C_A = C_L cos\alpha - C_D sin\alpha \quad (19)$$

2.3. Computational model, solver details, and boundary conditions

The GAMBIT code was used to discretize the computational domain into finite volume cells. The momentum and continuity equations were solved using Dirichlet boundary conditions, which are consistent with the Green-Gauss cell-based evaluation technique employed in the ANSYS FLUENT solver. Through a variety of tests using various interpolation approaches, the cell face values of the flow field variables as well as convergence conditions have been calculated. Based on its results, which were comparable to those of the third order MUSCL method, the second order upwind interpolation approach was then employed. As shown in Fig. (1), the grid distribution close to the square surface wall, the solution was seen to reach convergence when the scaled residuals approached 1×10^{-5}, where the flow field variables maintain constant values with successive iterations.

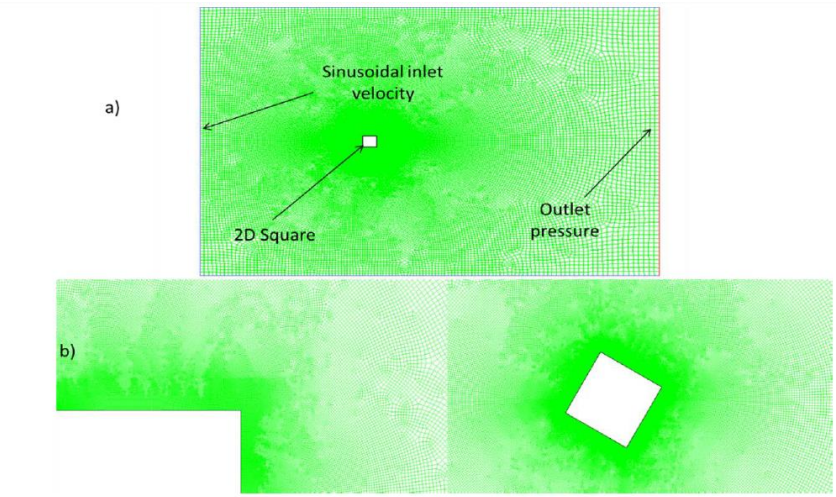

Figure 1: (a) Computational domain, and (b) computational grid near wall.

In this simulation, the axial flow of a square object was represented as a sinusoidal wave. The inlet velocity form, which was produced using Eq. (18), is displayed in Fig. (2). The inlet boundary conditions were adjusted to vary over time.

$$V = V_o + V_a(sin2\pi ft) \quad (18)$$

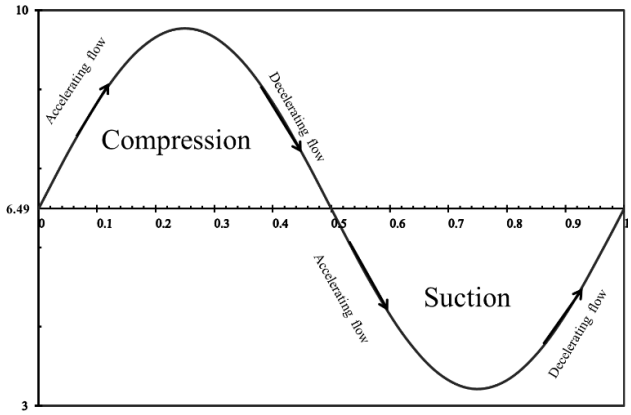

Figure 2: The sinusoidal wave boundary condition representing regular oscillating air input.

T. Nomura *et al.*'s experimental investigation [5] revealed that two instances of sinusoidal oscillating flows were produced. Table 1 lists these two flows' distinctive parameters. In order to meet the CFL (Courant Friedrichs Lewy) [21] requirement, the time step was set to 0.00056 seconds.

Table 1. Characteristic parameters of two experimental cases.

	Time period (sec)	*Vo (m/sec)*	*Va (m/sec)*
Case 1	0.5	6.64	**3.14**
Case 2	**1**	**6.49**	**3.19**

2.4. Grid Independence

The number of grid cells needed to guarantee that the model is free of numerical errors was estimated using multiple grids in order to reach a grid-independent test, as shown in Table 2. Grid D took less time than Grid C, yet both produced the same outcome. Thus, grid C is selected to carry out the study that follows.

Table 2. Specification of different grids used in the grid independence test.

Grid	*Number of Cells*	*First Cell*	*Growth Rate*	*EquiAngle Skew*
A	111803	1×10-4	1.02	**0.42**
B	202017	1×10-5	1.015	**0.465**
C	320451	1×10-5	1.012	**0.504**
D	**426878**	**1×10-6**	**1.01**	**0.501**

2.5. Solution validation

To provide the best agreement with the adopted experimental data, the oscillatory flow around the object was modeled using the realizable turbulence models [5]. Measurements are made of the unsteady forces operating on a square cylinder in an oscillating flow with a nonzero mean velocity. A special AC servomotor wind tunnel produces oscillating air flows. The velocity histories that are produced are nearly perfect sinusoidal waves. The Morison equation is compared with the measured unsteady forces. The following simulation instances used this data since it is the most experimental data with information accessible for the sinusoidal flow condition to confirm our work. The observed drag force from reference and the estimated drag force from CFD at two different frequencies exhibit excellent agreement, as shown in Figs. (3) and (4). Eq. (19) shows the Morison equation for the in-line force operating on the cylinder per unit length, which is used to calculate the drag force recorded.

$$F_D = \frac{1}{2}\rho B C_D |U| U + \rho A \tilde{C}_D \dot{U} \qquad (19)$$

Where $\dot{U}$= dU/dt and the unstable in-line force's inertia coefficient is represented by the non-dimensional coefficient $\tilde{C}_D$. The evaluation of this non-dimensional coefficient is contingent upon [22] and [23].

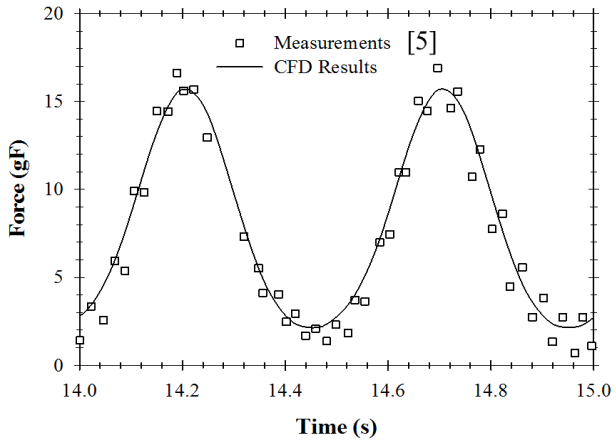

Figure 3: Computed using CFD with a frequency of 2 Hz and measured unsteady in-line force (angle of attack = 0 degree).

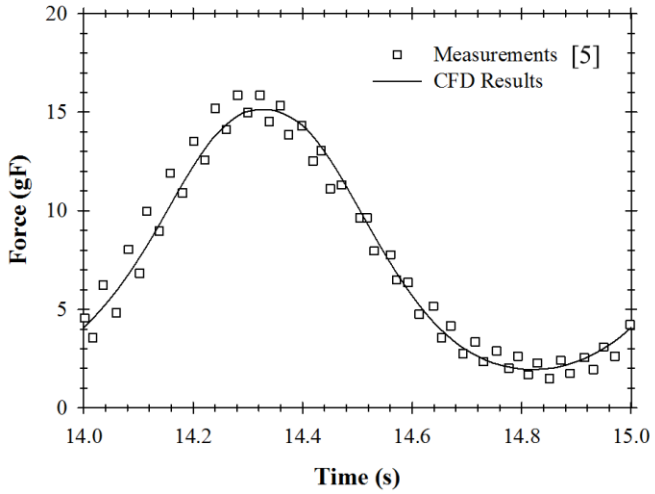

Figure 4: Unsteady in-line force was measured at a frequency of 1 Hz (angle of attack = 0 degrees) and computed using CFD.

3. RESULTS

3.1. Vortex shedding and turbulence

Fig. (5) presents the effect of the oscillating value of an incoming flow for compression and suction cycle. The contour of mean velocity magnitude at different time period shows low value around the object. But the lower and upper faces have high value area (1, 2) after this droop. The value in this area increased in acceleration period and then decreased in deceleration for compression cycle. On the other hand, the value in this area decreased in acceleration flow (creating a lower value at 0.627 second) and then increased in deceleration flow for suction cycle.

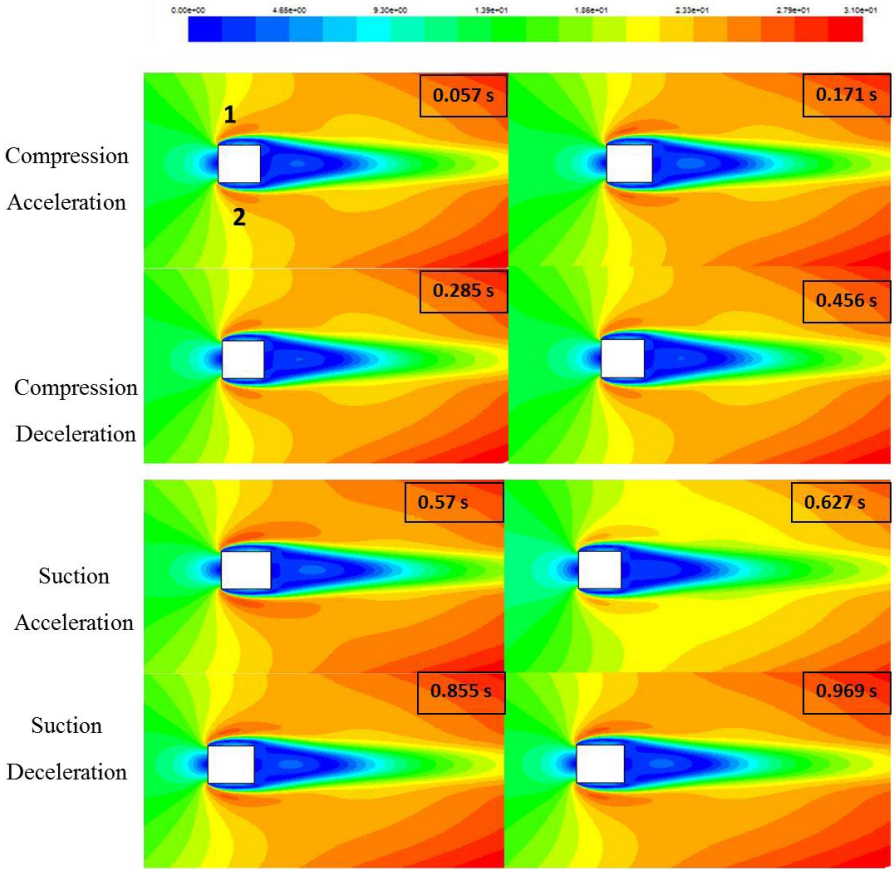

Figure 5: Contour of mean velocity magnitude in m/sec for sinusoidal input flow with frequency equal to 1 Hz.

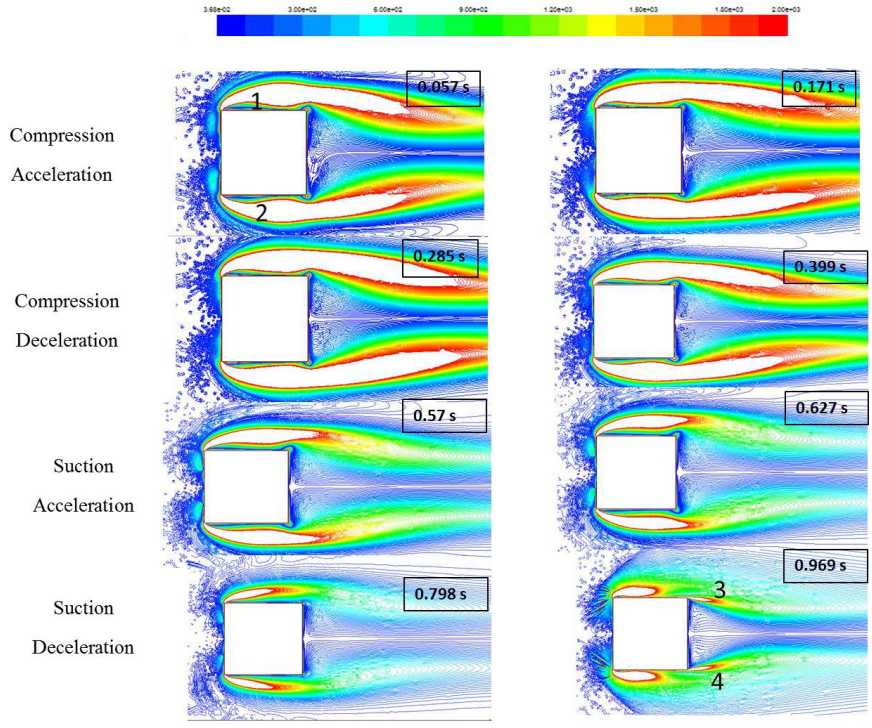

Figure 6: Contour of vorticity magnitude (m/s) for sinusoidal input flow with frequency equal to 1 Hz.

Fig. (7) displays the velocity vectors around the 2D square cylinder with varying rotational angles that are colored by the turbulent viscosity ratio. The turbulent viscosity ratio peaked at 10 degrees, as this figure illustrates. Moreover, the lowest values are obtained at 40 and 50 degrees.

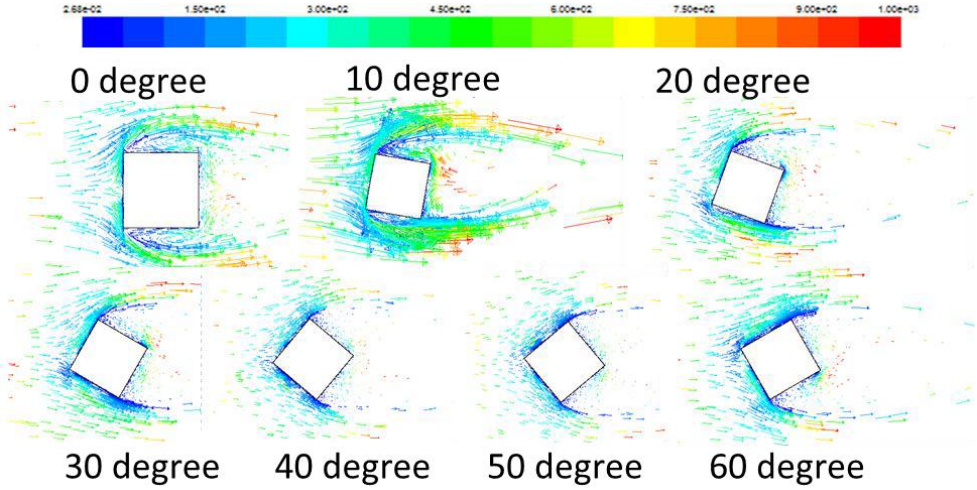

Figure 7: Velocity vectors for sinusoidal input flow with a frequency of 1 Hz and a velocity equal to 7.608204 m/s colored by the turbulent viscosity ratio at a certain period (0.057 seconds).

The contour of velocity colored by turbulent viscosity ratio around the 2D Square cylinder with different angle of rotation can be seen in Fig. (8). This figure shows four vortex areas (1, 2, 3, and 4). The construction of vortex in area 2 only changed with angle of rotation. On the other hand, the value of turbulent viscosity ratio in the four areas changed with angle of rotation. Maximum value for area 2 was created at 40 and 50 degrees. Maximum value for areas 3 and 4 was shown at 60 degrees.

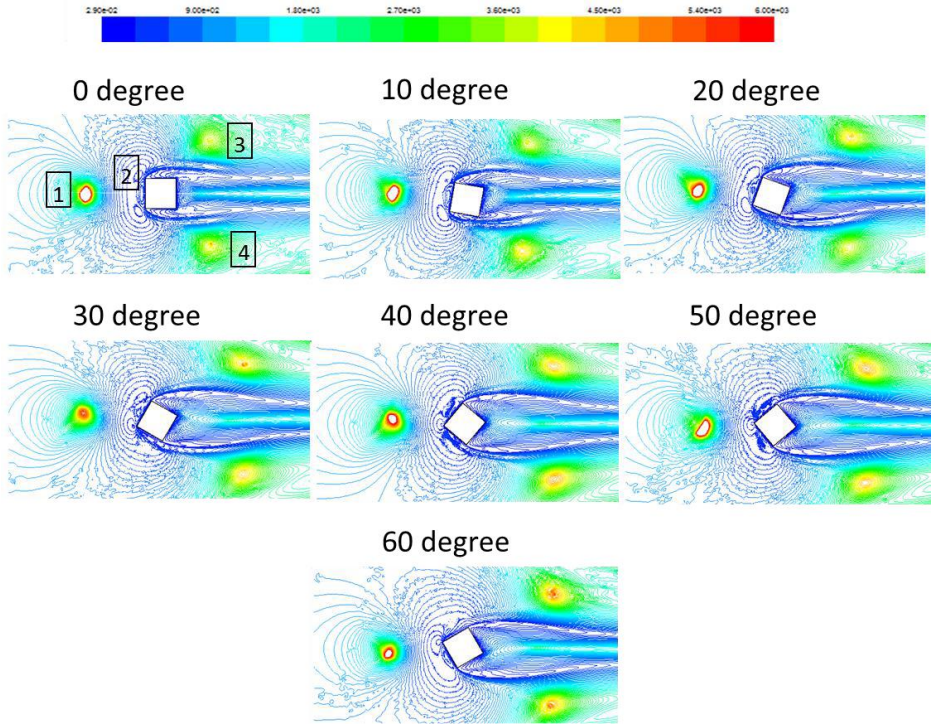

Figure 8: At a specific period (0.057 seconds), the turbulent viscosity ratio is used to color the velocity contours. For a sinusoidal input flow with a frequency of 1 Hz, the velocity is 7.608204 m/s.

The effect of change in the amplitude of axial velocity with the same frequency and initial velocity was presented in Fig. (9). With an axial velocity amplitude of 3.19 m/s and a Reynolds number of 2×10^4, the first figure displays two vortex zones (1, 2) on the upper and lower surfaces. The value of vorticity magnitude increases in tandem with the amplitude of axial velocity. A third area of vortex occurred in the bottom surface of the second figure, which shows an amplitude of axial velocity equal to 43.51 m/s with a Reynolds number of 1×10^5, and the third figure, which shows an amplitude of axial velocity equal to 110.51 m/s with a Reynolds number of 2.4×10^5.

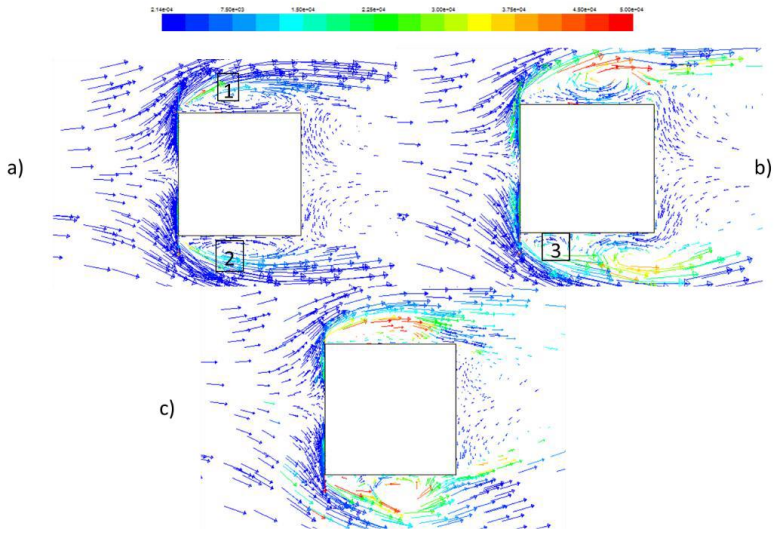

Figure 9: Velocity vectors colored by vorticity magnitude, (a) 3.19 m/s, Re = 2×10^4, (b) 43.51 m/s, Re = 2×10^4, and (c) 110.51 m/s, Re = 2.4×10^5, zero degree of rotaion, at certain time (0.176 second) for sinusoidal input flow with frequency equal to 1 Hz.

The object shape has the mean reason for the structures of vortex flow and flow turbulence. So, in Fig. (10), two different object shapes were presented. In the first figure for the square shape, it can be seen that there are four important areas. Area 1 has a very low velocity due to the collision by the object. Areas 2 and 3 have vortex flow and above this vortex there are high values of velocity. The back flow can be seen in area 4. For the circular in the second figure, the decrease in velocity value due to the collision was smaller than the square in area 1. Areas 2 and 3 have high value of velocity but without vortex flow. The back flow can see also in area 4.

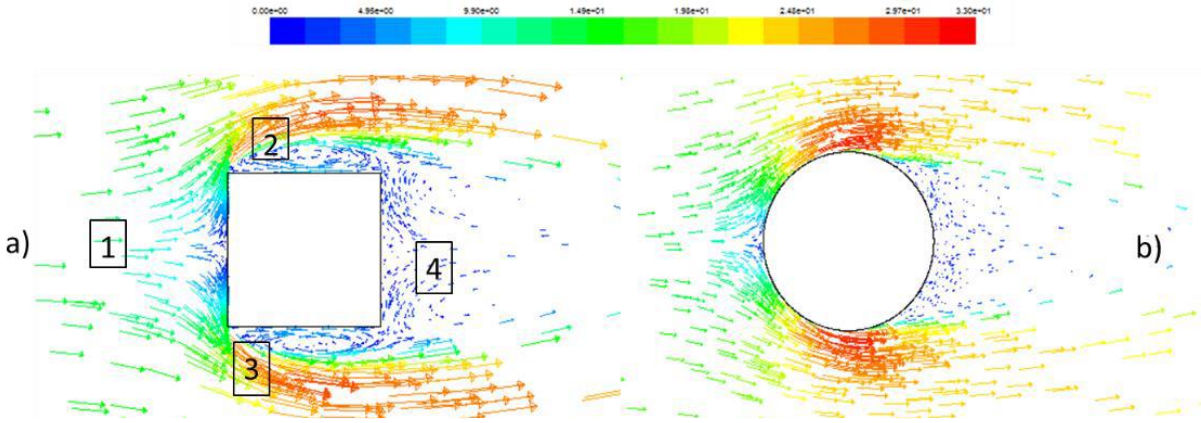

Figure 10: For a sinusoidal input flow with a frequency of 1 Hz, velocity vectors colored by velocity magnitude, (a) square, and (b) circular, with zero degree of rotation, at a certain period (0.176 seconds).

3.2. Hydrodynamic forces

The pressure coefficient for different incoming oscillating flow frequency (2, 1, 0.5, 0.25, 0.167) Hz, was presented in Fig. (11) for compression cycle and Fig. (12) for suction cycle. It is evident from Fig. (11) that the pressure coefficient rises in tandem with the flow frequency. With the exception of the pressure coefficient, which was roughly similar to the value at 0.167 Hz at 0.5 Hz. Furthermore, in Fig. (12), for suction cycle, the value of pressure coefficient was smaller than value for compression cycle at the same condition (by approximately seven times at maximum value and by approximately twenty times at minimum value). Also, the increase in flow frequency comes with an increase in the pressure coefficient. Except the pressure coefficient at 1 Hz, was approximately less than the value at 0.5 Hz.

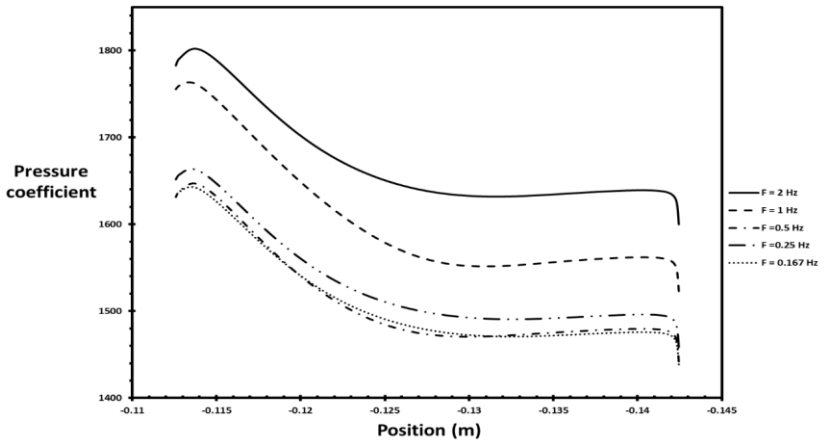

Figure 11: Pressure coefficient for the upper surface in compression cycle with zero degree of rotation at maximum velocity (about equal to 9.5 m/s) with varying incoming oscillatory flow frequencies (2, 1, 0.5, 0.25, and 0.167) Hz.

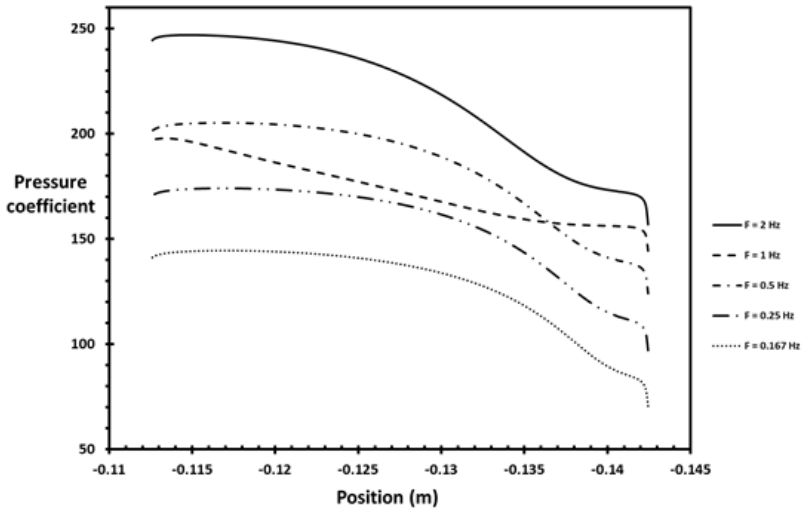

Figure 12: Pressure coefficient at zero degree of rotation at maximum velocity (about equivalent to 9.5 m/s) for upper surface in compression cycle, and for various incoming oscillating flow frequencies (2, 1, 0.5, 0.25, and 0.167) Hz.

The impact of various rotational angles on the lift and drag force coefficients is depicted in Fig. (13). In both cycles, a 10-degree rotation angle yields the lowest lift force coefficient value. As a result, in both cycles, the left force coefficient's maximum value was produced at a 30-degree rotational angle.

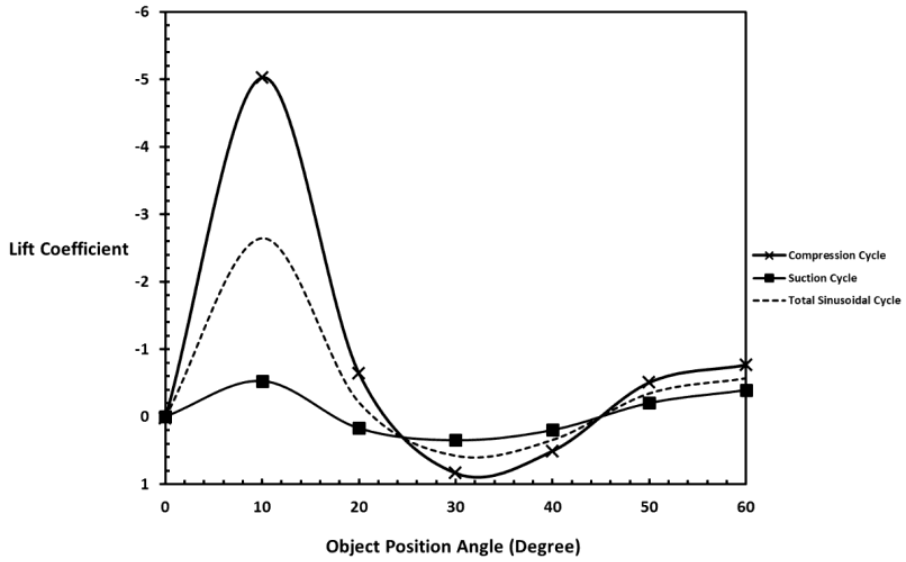

Figure 13: Lift coefficient for different rotation angle (0, 10, 20, 30, 40, 50 and 60) degree, at max velocity (approximately equal to 9.5 m/s) for sinusoidal input flow with frequency equal to 1 Hz.

On the other hand, in Fig. (14), for the drag force coefficient, the maximum value was created at 50 degrees and the minimum at 0-degree rotation angle in both cycles.

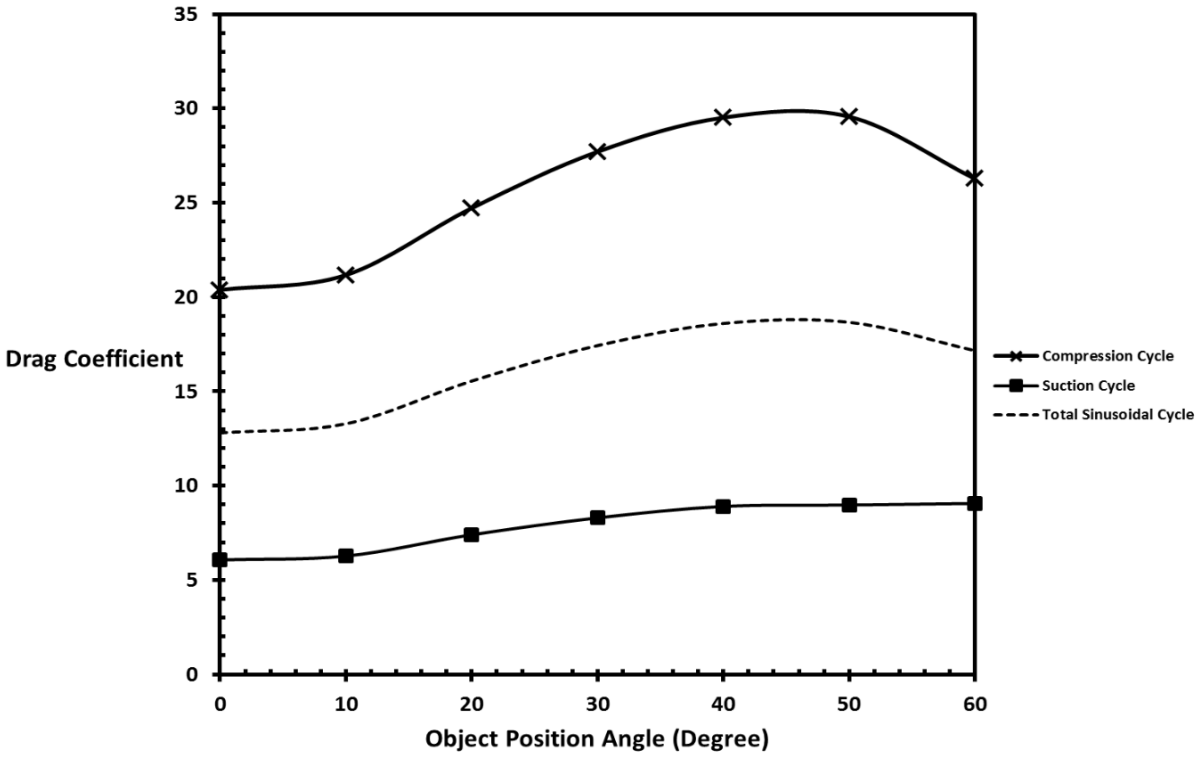

Figure 14: Drag coefficient for different rotation angle (0, 10, 20, 30, 40, 50 and 60) degree, at max velocity (approximately equal to 9.5 m/s) for sinusoidal input flow with frequency equal to 1 Hz.

The torque coefficient variation brought on by various rotational angles is shown in Fig. (15). The torque coefficient is at its highest for compression and suction cycles when the object position angle is zero degrees. Additionally, a minimum value of 50 degrees for the compression cycle and 60 degrees for the suction cycle were established.

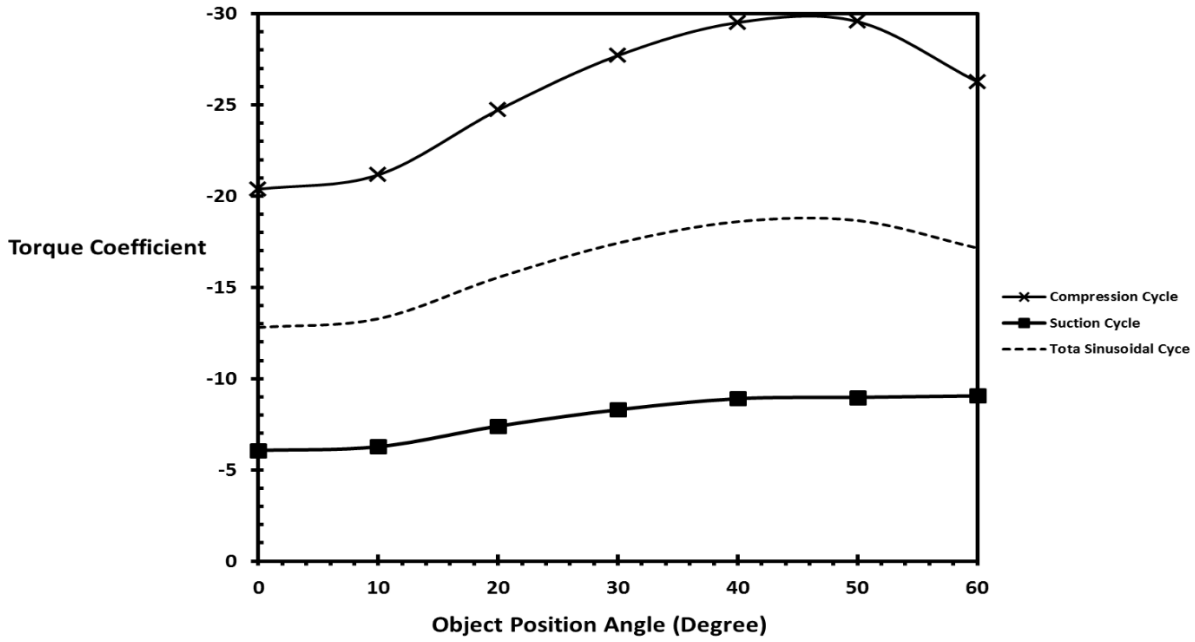

Figure 15: The torque coefficient for a sinusoidal input flow with a frequency of 1 Hz at maximum velocity (about equivalent to 9.5 m/s) for various rotation angles (0, 10, 20, 30, 40, 50, and 60 degrees).

As seen in Fig. (16), a rotation angle of 10 degrees yields the lowest value for the axial force coefficient in both cycles. Otherwise, in both cycles, the 30-degree rotational angle produced the highest value of the axial force coefficient.

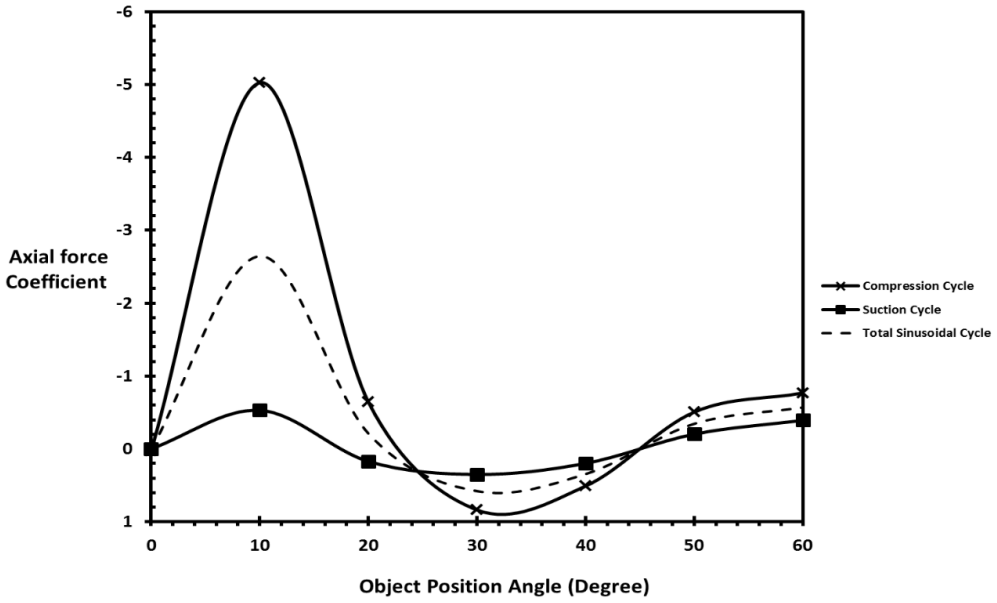

Figure 16: The axial force coefficient for a sinusoidal input flow with a frequency of 1 Hz at maximum velocity (about equivalent to 9.5 m/s) for various rotation angles (0, 10, 20, 30, 40, 50, and 60 degrees).

3.3. Second law analysis

The entropy generation in the flow over the square is directly impacted by the change in the rotational angle. Nevertheless, the flow over the square exhibits a distinct entropy generation signature at varying angles, as illustrated in Fig. (17). Ten degrees is the minimum value for both compression and suction cycles. Furthermore, the global entropy generation rate for suction cycles was consistently lower than that for compression cycles. The global entropy generation for the whole sinusoidal cycle is displayed in Fig. (18).

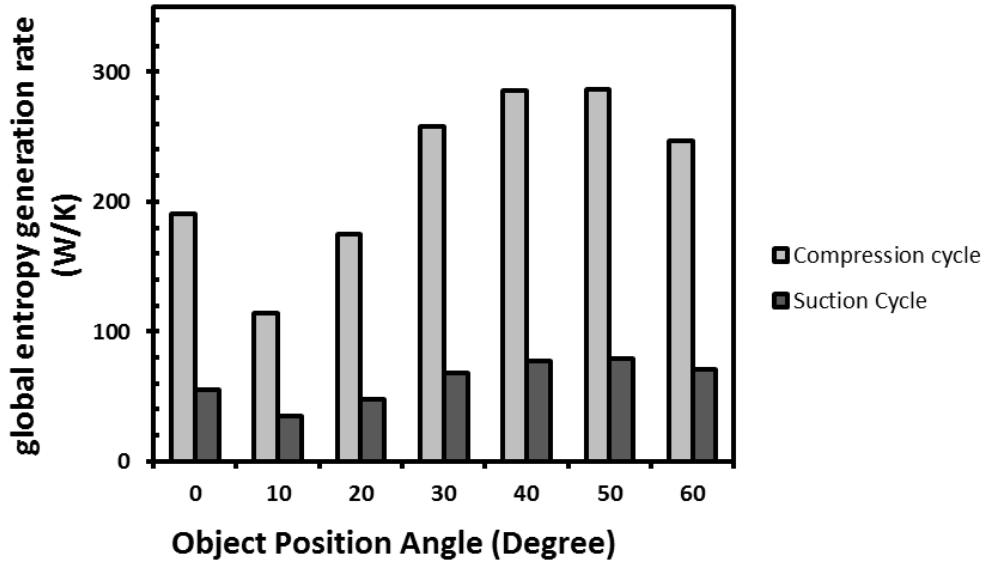

Figure 17: At a maximum velocity of 9.5 m/s for sinusoidal flow with a frequency of 1 Hz for compression and suction cycles, the global entropy generation rate is calculated for various rotation angles (0, 10, 20, 30, 40, 50, and 60 degrees).

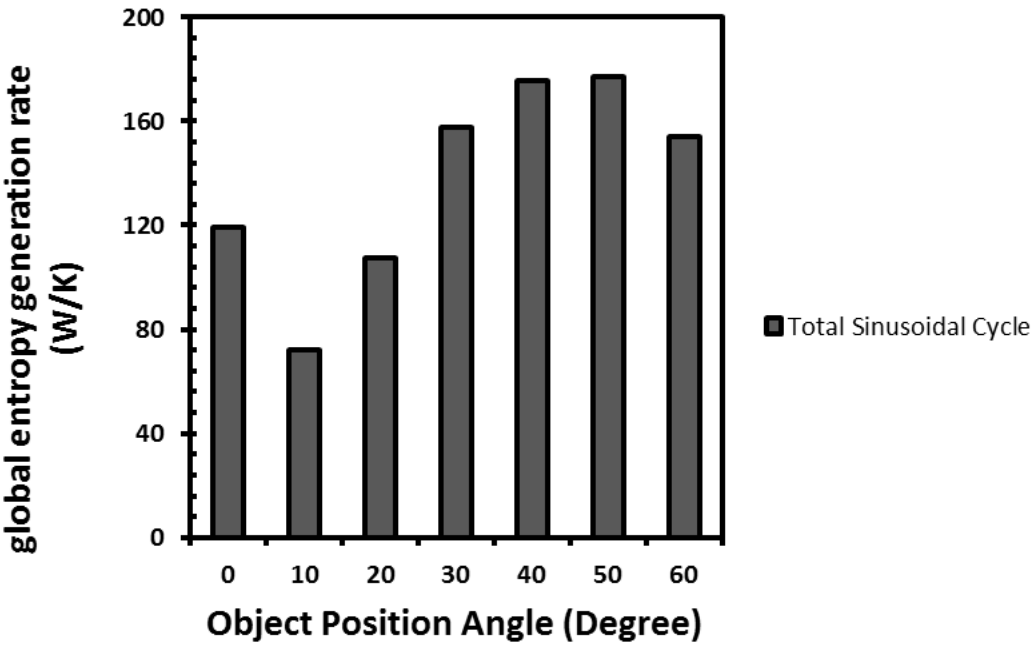

Figure 18: The global entropy generation rate for sinusoidal flow with a frequency equal to 1 Hz throughout the whole sinusoidal cycle at a maximum velocity of 9.5 m/s for various rotation angles (0, 10, 20, 30, 40, 50, and 60 degrees).

Figures (19) and (20) showed the global entropy generation rate for various incoming oscillating flow frequencies. Similar to the influence of the angle of rotation, the entropy generation is directly impacted by the various incoming oscillatory flow frequencies. It can demonstrate that a drop in the global entropy generation rate coincides with a drop in flow frequency. In all compression and suction cycles, it was greater than the value at 2 Hz, with the exception of the value at 1 Hz.

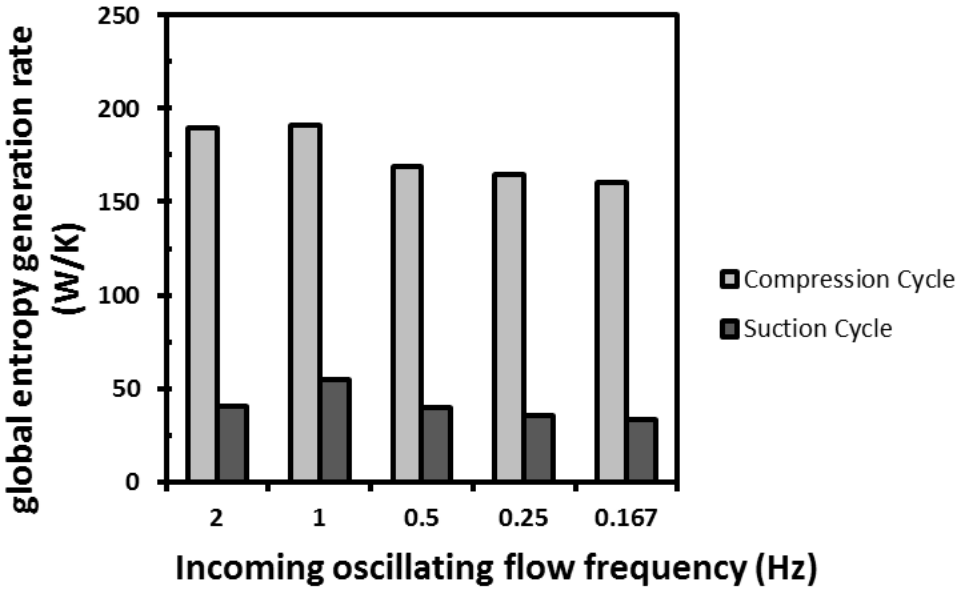

Figure 19: The global entropy production rate for compression and suction cycles at zero degree of rotation and maximum velocity (about 9.5 m/s) at various incoming oscillating flow frequencies (2, 1, 0.5, 0.25, and 0.167 Hz).

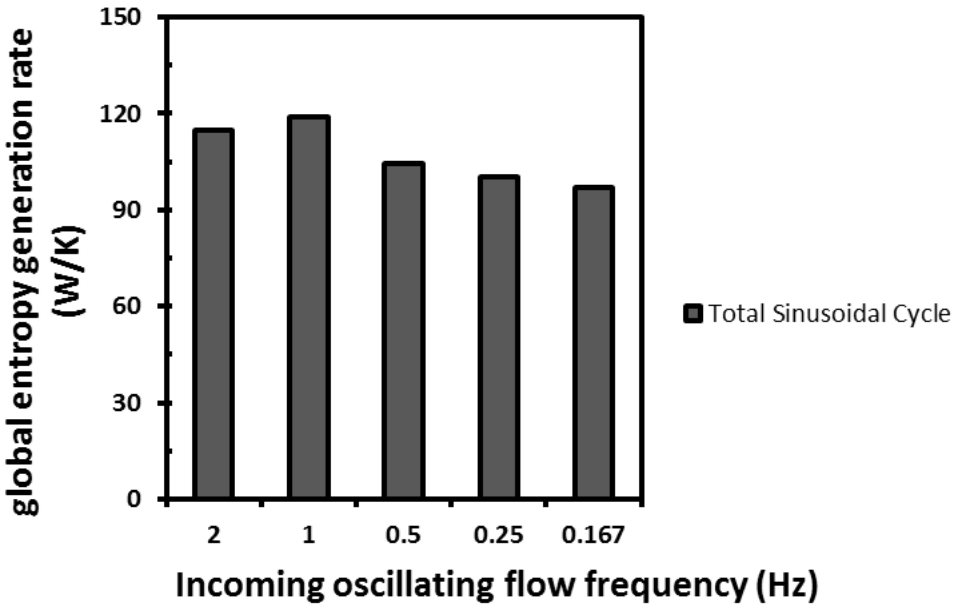

Figure 20: The global entropy generation rate for different incoming oscillating flow frequency (2, 1, 0.5, 0.25, and 0.167 Hz) for the total sinusoidal cycle.

4. CONCLUSIONS

In order to better understand how the object rotation angle influences the flow characteristics around the cylinder and the resulting induced hydrodynamic forces, as well as the frequency of the incoming flow, the amplitude of axial velocity, frequency, and object shape, this paper examines two-dimensional incompressible unsteady flow simulations of a square cylinder under sinusoidal flow boundary conditions. According to the results, a high flow frequency results in a high-pressure coefficient. At a rotation angle of 10 degrees, the lift and drag coefficients are at their lowest, while at 30 degrees, they reach their maximum. The outcome also shows that the total rate of entropy formation in the flow around a square cylinder is fundamentally influenced by the object rotation angle

and the incoming flow frequency. where a rotation angle of 10 degrees and a flow frequency of 0.167 Hz caused the lowest value to accumulate.

5. REFERENCES

1. T. Sarpkaya, "Force on a circular cylinder in viscous oscillatory flow at low Keulegan—Carpenter numbers," *Journal of Fluid Mechanics,* vol. 165, pp. 61-71, 1986, doi: 10.1017/S0022112086002999.
2. E. D. Obasaju, P. W. Bearman, and J. M. R. Graham, "A study of forces, circulation and vortex patterns around a circular cylinder in oscillating flow," *Journal of Fluid Mechanics,* vol. 196, pp. 467-494, 1988, doi: 10.1017/S0022112088002782.
3. C. H. K. Williamson, "Sinusoidal flow relative to circular cylinders," *Journal of Fluid Mechanics,* vol. 155, pp. 141-174, 1985, doi: 10.1017/S0022112085001756.
4. T. Chi Chao and N. E. Huang, "Combined effects of current and waves on fluid force," *Ocean Engineering,* vol. 2, no. 4, pp. 183-193, 1973/06/01/ 1973, doi: https://doi.org/10.1016/0029-8018(73)90004-8.
5. T. Nomura, Y. Suzuki, M. Uemura, and N. Kobayashi, "Aerodynamic forces on a square cylinder in oscillating flow with mean velocity," *Journal of Wind Engineering and Industrial Aerodynamics,* vol. 91, no. 1, pp. 199-208, 2003/01/01/ 2003, doi: https://doi.org/10.1016/S0167-6105(02)00345-8.
6. D. Yeo and N. P. Jones, "Aerodynamic forces induced by vertically oscillating incoming flow on a yawed horizontal circular cylinder," *Journal of Wind Engineering and Industrial Aerodynamics,* vol. 104-106, pp. 188-195, 2012/05/01/ 2012, doi: https://doi.org/10.1016/j.jweia.2012.02.032.
7. L. Shen and E.-S. Chan, "Numerical simulation of oscillating flows over a bed-mounted circular cylinder," *Applied Ocean Research,* vol. 32, no. 2, pp. 233-241, 2010/04/01/ 2010, doi: https://doi.org/10.1016/j.apor.2009.11.001.
8. A. K. Saha, "Unsteady flow past a finite square cylinder mounted on a wall at low Reynolds number," *Computers & Fluids,* vol. 88, pp. 599-615, 2013/12/15/ 2013, doi: https://doi.org/10.1016/j.compfluid.2013.10.010.
9. A. Okajima, T. Matsumoto, and S. Kimura, "Force Measurements and Flow Visualization of Circular and Square Cylinders in Oscillatory Flow," *JSME International Journal Series B,* vol. 41, no. 4, pp. 796-805, 1998, doi: 10.1299/jsmeb.41.796.
10. T. S. Sarpkaya, "Forces on Cylinders Near a Plane Boundary in a Sinusoidally Oscillating Fluid," *Journal of Fluids Engineering-transactions of The Asme,* vol. 98, pp. 499-503, 1976.
11. T. Sarpkaya, "In - Line And Transverse Forces, On Cylinders In Oscillatory Flow At High Reynolds Numbers," presented at the Offshore Technology Conference, 1976. [Online]. Available: https://doi.org/10.4043/2533-MS.
12. T. Sarpkaya and F. Rajabi, "Hydrodynamic Drag On Bottom-Mounted Smooth And Rough Cylinders In Periodic Flow," presented at the Offshore Technology Conference, 1980. [Online]. Available: https://doi.org/10.4043/3761-MS.
13. Y. Liu, R. M. C. So, and Z. X. Cui, "A finite cantilevered cylinder in a cross-flow," *Journal of Fluids and Structures,* vol. 20, no. 4, pp. 589-609, 2005/05/01/ 2005, doi: https://doi.org/10.1016/j.jfluidstructs.2005.02.009.
14. D. Farivar, "Turbulent uniform flow around cylinders of finite length," *AIAA Journal,* vol. 19, no. 3, pp. 275-281, 1981/03/01 1981, doi: 10.2514/3.7771.
15. B. E. Launder and D. B. Spalding, "The numerical computation of turbulent flows," *Computer Methods in Applied Mechanics and Engineering,* vol. 3, no. 2, pp. 269-289, 1974/03/01/ 1974, doi: https://doi.org/10.1016/0045-7825(74)90029-2.
16. D. Wilcox, *Turbulence Modeling for CFD (Third Edition) (Hardcover)*. 2006.
17. C. Hirsch, "Numerical Computation of Internal and External Flows: The Fundamentals of Computational Fluid Dynamics," *Numerical Computation of Internal and External Flows: The Fundamentals of Computational Fluid Dynamics,* 01/01 2007, doi: 10.1016/B978-0-7506-6594-0.X5037-1.

18. A. Bejan, "Entropy generation minimization: The new thermodynamics of finite-size devices and finite-time processes," *Journal of Applied Physics,* vol. 79, no. 3, pp. 1191-1218, 1996, doi: 10.1063/1.362674.
19. C. Iandoli and S. Enrico, "3-D Numerical Calculation of the Local Entropy Generation Rates in a Radial Compressor Stage," *International Journal of Thermodynamics,* vol. 8, 06/01 2005, doi: 10.5541/ijot.148.
20. R. E. Sheldahl and P. C. Klimas, "Aerodynamic characteristics of seven symmetrical airfoil sections through 180-degree angle of attack for use in aerodynamic analysis of vertical axis wind turbines," United States, 01 1981. [Online]. Available: https://www.osti.gov/biblio/6548367 https://www.osti.gov/servlets/purl/6548367
21. C. A. d. Moura and C. S. Kubrusly, *The Courant-Friedrichs-Lewy (CFL) Condition: 80 Years After Its Discovery*. Birkhäuser Basel, 2012.
22. A. Okajima, T. Matsumoto, and A. Kondo, "Force Measurements of Two Circular Cylinders in Oscillatory Flow," *The proceedings of the JSME annual meeting,* vol. 2000.1, pp. 897-898, 07/31 2000, doi: 10.1299/jsmemecjo.2000.1.0_897.
23. M. P. Norton, "Flow-induced vibration: 2nd edition, R.D. Blevins, Van Nostrand Reinhold, New York, 1990, 451 pages, $59.95," Experimental Thermal and Fluid Science, vol. 4, no. 1, pp. 135-136, 1991/01/01/ 1991, doi: https://doi.org/10.1016/0894-1777(91)90027-O.